Instability driven by settling and evaporation in a shear flow: A model for asperitas clouds

S. Ravichandran [*]

Nordita, KTH Royal Institute of Technology and Stockholm University, Stockholm, Sweden SE-10691

Rama Govindarajan[†]

International Centre for Theoretical Sciences, Bengaluru 560089, India

We study, by direct numerical simulations in two and three dimensions, the instability caused by the settling and evaporation of water droplets out of a cloudy layer saturated with vapor into a dry subcloud ambient under conditions where mammatus clouds were shown to form but with the addition of background shear. We show that shear changes the type of cloud formation qualitatively from mammatus-like to a newly identified cloud type called asperitas. Intermediate levels of shear are shown to be needed. Shear suppresses the growth of small-scale perturbations, giving rise to smooth, long-lasting structures and smaller rates of mixing. Three-dimensionality is shown to make a qualitative difference, unlike in mammatus clouds. We also show that under non-cloud-like conditions, the instability can be very different.

I. INTRODUCTION

The distinctive shapes that atmospheric clouds take make them an artist's delight. Among the most visually stunning of the various cloud types are mammatus clouds, which are pendulous blobs of cloud fluid suspended, as it were, from the sky. Mammatus clouds are typically seen underneath cumulonimbus anvils, although they also are known to form elsewhere. Several explanations for their formation, and for their characteristic appearance, have been proposed, including layer subsidence, radiative cooling, and the evaporation of ice particles and/or water droplets settling out of the cloud. See Ref. [1] for a comprehensive review and Refs. [2,3] for numerical simulations of mammatus clouds suggesting that the cooling of the subcloud air plays a crucial role in the formation of mammatus clouds. It has also been suggested that mammatus clouds are simply the descending part of the circulation created due to the radiative temperature difference between the lower boundary of the cloudy layer and the subcloud dry air [4]. Ravichandran *et al.* [5] (hereafter RMG20) proposed that mammatus clouds form due to the settling of liquid droplets into the dry air layers beneath the cloud, resulting in evaporative cooling of this layer, and setting into motion a Rayleigh-Taylor-type instability. They studied the role of droplet size and liquid water content on the lobe sizes that can result using linear stability analysis and direct numerical simulations, finding that lobelike instabilities result only for sufficiently large droplet sizes as well as large liquid water content. It has been pointed out, however, that none of the proposed mechanisms explains every observation of mammatus clouds and therefore that more than one mechanism can cause lobelike clouds that may be called mammatus [1].

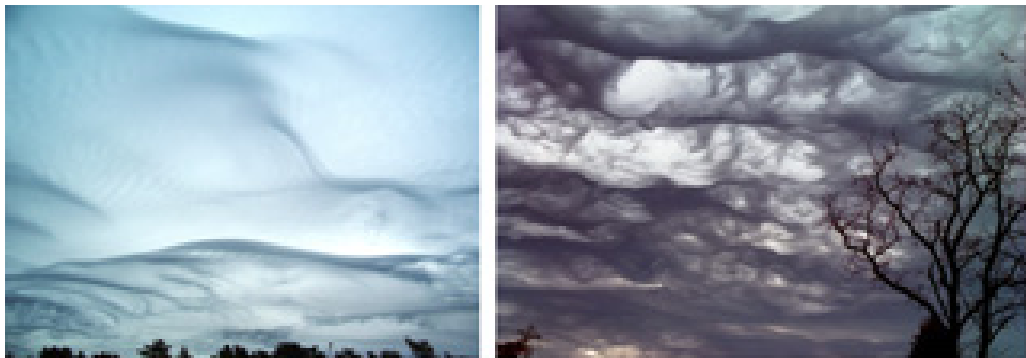[*]ravichandran@su.se

[†]rama@icts.res.in

FIG. 1. Left: Asperitas clouds over Tallinn, Estonia, on April 9th, 2009. By Ave Maria Mõistlik, Own work, CC BY-SA 3.0 [7]. Right: Asperitas clouds over Pocahontas, Missouri, on August 9th, 2008. By Agathaman, Own work, CC BY-SA 3.0 Unported [8].

In the year 2017, for the first time in nearly six decades, the World Meteorological Organisation (WMO) designated a new cloud type called "asperitas" [6], from the Latin for "severity," described to be "well-defined, wave-like structures in the underside of the cloud; more chaotic and with less horizontal organization than the variety undulatus. Asperitas is characterized by localized waves in the cloud base, either smooth or dappled with smaller features, sometimes descending into sharp points, as if viewing a roughened sea surface from below." The wavelike nature and the descent into sharp points suggest that their creation process could be related to that of mammatus clouds. They, however, look wavy rather than bloblike and the lobes are inclined to the vertical. Two typical examples, pictures available in the public domain, are reproduced in Fig. 1. Several more may be found on the website of the Cloud Appreciation Society (whose efforts were responsible for the designation of asperitas as a separate cloud type; see Ref. [9]). A stunning timelapse of asperitas evolution may be found in Ref. [10].

The only paper we can find on asperitas clouds is Ref. [11] (hereafter GH17), based on a dissertation by one of the paper's authors. GH17 find that in the few complete observations of asperitas clouds available, the Richardson number $\mathrm{Ri} = N^2/S^2 > 0.25$, where N is the Brunt-Väisälä frequency and S the shear rate, is too large for the Kelvin-Helmholtz instability to be active. They mainly study observations and also perform some idealized large eddy simulations using radiosonde profiles associated with the observations of asperitas as initial conditions. They propose that layers of stratification within the cloud can give rise to ducted gravity waves under certain conditions and that this could form asperitas clouds aided by differential shear in the layers. We propose a different mechanism for the formation of asperitas clouds based on turbulence and cloud microphysics by the settling and evaporation of water droplets in a background shear. The thermodynamics of phase change is an important ingredient in our mechanism. Since this cloud type is only recently identified, further work will be needed to critically examine the applicability of each of these two mechanisms and perhaps others. We begin by discussing settling-driven instabilities in various contexts without phase change.

Fluid dynamical systems with multiple scalar components where one of the scalar components has a finite settling velocity (typically because it is a suspended phase) occur frequently in geophysics. For instance, in estuaries where silt-laden river water flows into the sea, the rate of mixing of the fresh water into the saline water is mediated by the settling driven instability at the interface (see, e.g., Refs. [12–15]). Settling driven instabilities (with the additional complexity of coagulation and a changing diffusivity of the suspended phase) are also responsible for layer formation in volcanic ash mushroom clouds [16,17] and the significant increase in the lifetime of such ash clouds that results.

As we shall see, settling-driven instabilities are broadly related to double-diffusive (DD) instabilities, where the system in the base state is nominally stably stratified, but instabilities occur because

of differential diffusion of different scalars in the flow. The difference is that in the typical DD system, none of the scalar components undergoes settling. Both DD and settling driven instabilities have been studied in the presence of a horizontal shear flow [18–21]. In general, due to the imposed homogeneity in the direction of flow, shear stabilizes the fingering instabilities that occur at the interface, while modes in the direction perpendicular to the shear are unaffected. In double-diffusive systems, this leads to the formation of "salt sheets" which have been observed experimentally and in simulations, reducing the vertical fluxes of heat and salinity (see, e.g., Ref. [18]).

Here we study the influence of shear on the lobelike instabilities that arise due to the settling and evaporation of water droplets. Our system has two nonsettling scalar components, namely temperature and water vapor, in the ambient fluid (air) and liquid droplets which settle under gravity and undergo evaporation as they do so. Without a base shear, mammatus clouds form under a range of physical parameters, and in a certain range of shear, we propose that our mechanism supports the formation of asperitas clouds.

We employ the formulation used in RMG20 and coarse-grain the liquid water droplets into a scalar field with a finite settling velocity which can vary in space and time. We perform direct numerical simulations (DNS) of the governing equations in two and three dimensions, with the interface between cloudy and clear air initially perturbed sinusoidally with a given single wavelength and an externally imposed shear flow maintained by upper and lower boundaries that move in opposite directions, and present results from these simulations.

The rest of the paper is organized as follows. In Sec. II, we describe the geometry of the problem and outline the derivation of the governing equations. We then nondimensionalize the equations and list the governing nondimensional parameters. In Sec. III, we present and discuss results from DNS in two and three dimensions (2D and 3D), showing that the extra spatial dimension changes the dynamics qualitatively when shear is nonzero. We then conclude in Sec. IV with some thoughts on future work.

II. PROBLEM SETUP AND NUMERICAL SIMULATION

We devise the simplest initial scenario for the formation of asperitas clouds, shown schematically in Fig. 2. The geometry is a rectangular or cuboidal volume of dimensions L_x, (L_y), L_z. We show L_y in brackets since it appears in our three-dimensional simulations, whereas our two-dimensional simulations are in the x-z plane. The domain consists of a layer of cloud fluid placed above a layer of dry air. The cloud fluid is a mixture of dry air, water vapor, and liquid water droplets. Initially, the mean location of the interface between cloudy and clear air is z_0. The entire system is under constant shear $\tilde{S}$, with the initial horizontal component of velocity u varying linearly with the vertical coordinate as

$$u(z, t = 0) = \tilde{S}(z_0 - z). \tag{1}$$

On the lower and upper boundaries, at $z = 0$ and $z = L_z$, respectively, we apply horizontal velocity boundary conditions matching the shear profile, along with setting the spanwise and vertical velocities v and w to be zero:

$$u(z = 0) = \tilde{S}z_0$$
$$u(z = L_z) = -\tilde{S}(L_z - z_0)$$
$$v(z = 0) = v(z = L_z) = w(z = 0) = w(z = L_z) = 0. \tag{2}$$

The horizontal directions are periodic. The system is initially isothermal, with the temperature $T = T_b$ everywhere, and the initial vapor concentration in the cloud layer is set at the saturation value for this temperature. The interface at $z = z_0$ is initially perturbed sinusoidally with an amplitude $h/2$ and wavelengths λ_x and λ_y in the x and y directions respectively [in 2D, the last factor in (3) is set
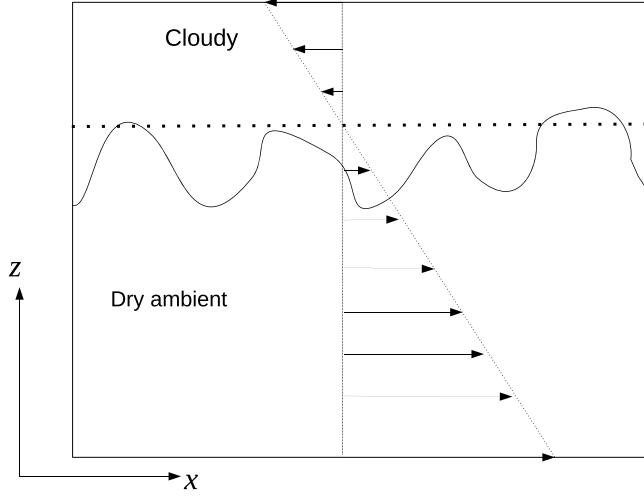
FIG. 2. The geometry of the problem, shown here in two dimensions. The background shear is linear, with zero velocity at the location $z = z_0$ (the dotted line) and the velocity for $z < z_0$ chosen to be positive in the x direction. At the initial time, the region $z > z_0$ contains water vapor at saturation and liquid water droplets, whereas the domain below z_0 is dry. The interface is initially perturbed (solid wavy line) as discussed in the text. Gravity points in the $-z$ direction

identically to unity]:

$$z_i = z_0 + \frac{h}{2}\sin\left(\frac{2\pi x}{\lambda_x}\right)\sin\left(\frac{2\pi y}{\lambda_y}\right), \tag{3}$$

with the region $z > z_i$ containing saturated vapor and liquid water droplets and $z < z_i$ consisting of dry air. The water droplets of initial radius a_0 and number density n in the cloudy part of the domain, represented here in coarse-grained form by a liquid field. The quantities of vapor and liquid water are given in term of their normalized mixing ratios (mass of vapor-liquid per unit mass of dry air):

$$r_{v,l} = \frac{\tilde{r}_{v,l}}{r_s^0} = \frac{\rho_{v,l}}{\rho_d r_s^0}, \tag{4}$$

where $\rho_{v,l}$ are the densities of vapor and liquid and ρ_d is the density of dry air. We have normalized the mixing ratios $\tilde{r}_{v,l}$ using $r_s^0 = \rho_s^0/\rho_d$ and the saturation vapor mixing ratio at the base temperature T_b (see RMG20 for a more detailed discussion). The deviation from T_b everywhere in the flow is represented by a nondimensional temperature,

$$\theta = \frac{T - T_b}{\Delta T}. \tag{5}$$

We thus have, at $t = 0$,

$$r_{v,0}(z) = \begin{cases} 1 & z \geqslant z_i \\ 0 & z < z_i \end{cases}, \tag{6}$$

$$r_{l,0}(z) = \begin{cases} r_l^0 + \text{noise} & z \geqslant z_i \\ 0 & z < z_i \end{cases}, \tag{7}$$

and

$$\theta_0 = 0. \tag{8}$$

The subscript 0 indicates a quantity at time $t = 0$.

We assume that the water droplets are small enough $[\mathcal{O}(10)\mu\text{m}]$ to remain spherical and obey the Stokes drag law. They therefore settle with a finite instantaneous velocity,

$$v_p(a) = \frac{2g\rho_w}{9\nu\rho_d}a^2, \tag{9}$$

where a is the instantaneous droplet radius and g is the acceleration due to gravity. We note that droplet sizes observed in real asperitas clouds (which, from the very limited observations available [22], seem to form under similar atmospheric conditions as mammatus) are larger, and the Stokes law, Eq. (9), will need higher-order corrections. Large droplets are also subject to inertial effects, which cause the droplets to deviate from fluid streamlines, with the droplet velocities $\boldsymbol{v}$ given by

$$\boldsymbol{v} = \boldsymbol{u} - \frac{v_p}{g}\frac{D\boldsymbol{u}}{Dt},$$

where D/Dt is the material derivative following fluid streamlines and we have expanded the Maxey-Riley equations [23] for a heavy particle to first order in the particle timescale $\tau_p = v_p/g$ (which is small relative to the flow timescales). Here, following Refs. [13–15], we ignore these effects, while retaining the settling velocity of the droplets.

As in RMG20, we assume that n is constant everywhere, i.e., as droplets evaporate, their number density remains constant even as their radii shrink. The instantaneous radius of the droplets is prescribed by its representative value $a = [3\rho_l/(4\pi n)]^{1/3}$ inside each grid cell. We note that droplet radii are far smaller than the Kolmogorov scale, and in a typical cloud, the number density is $O(1)$ in a cube whose side is the Kolmogorov scale. The same number density is prescribed nominally in the initially dry region in the lower half of the domain, although wherever $r_l = 0$, it does not affect the dynamics. Droplets evaporate on a timescale [see also Eq. (16) below]

$$\tilde{\tau}_s = \frac{Cr_s^0\rho_d}{4\pi na} = \frac{C\rho_w}{3}\frac{a^2}{r_l}, \tag{10}$$

where r_l is the normalized liquid mixing ratio [Eq. (4)] and C is a dimensional constant whose value is about 10^7 s m kg^{-1} in a cloud. The velocity scaling emerges from considering the droplets as spheres in the Stokesian limit, whereas the evaporation timescale arises from assuming purely diffusive vapor flux from isolated spherical droplets (e.g., Ref. [24]). As they settle out of the cloud into the dry ambient, droplets evaporate, cooling, and humidifying the subsaturated air underneath the cloudy layer.

The governing equations are the Boussinesq Navier-Stokes equations with advection-diffusion equations for θ, r_v, and r_l. To nondimensionalize the equations, we must define a length scale. The total height of the cloud layer could be a possibility, but this height does not directly influence the physics under consideration. We therefore choose the end-to-end initial perturbation amplitude h as the length scale. The initial settling velocity $v_{p,0}$ provides a natural velocity scale, giving a timescale $h/v_{p,0}$. The nondimensional governing equations are

$$\nabla \cdot \boldsymbol{u} = 0, \tag{11}$$

$$\frac{D\boldsymbol{u}}{Dt} = -\nabla p + \frac{1}{\text{Re}}\nabla^2\boldsymbol{u} + \frac{\boldsymbol{e}_z}{\text{Fr}^2}\big[\theta + r^0(\chi r_v - r_l)\big], \tag{12}$$

$$\frac{D\theta}{Dt} = \frac{1}{\text{Re}}\nabla^2\theta + L_1 C_d, \tag{13}$$

$$\frac{Dr_v}{Dt} = \frac{1}{\text{Re}}\nabla^2 r_v + C_d, \tag{14}$$

$$\frac{Dr_l}{Dt} = C_d + \frac{v_p}{v_{p,0}}\frac{\partial r_l}{\partial z}, \tag{15}$$

where $r^0 = r_s^0 T_b/\Delta T$ is a ratio of buoyancy contributions from water substance and temperature, $1 + \chi = 28.9/18 \approx 1.6$ is the ratio of molecular masses of air and water vapor, and C_d is the nondimensional rate of condensation,

$$C_d = \frac{dr_l}{dt} = \frac{\mathcal{H}(r_v, r_l, r_s)}{\tau_s}\left(\frac{r_v}{r_s} - 1\right), \tag{16}$$

where $\tau_s = \tilde{\tau}_s v_{p,0}/a_0$ denotes the instantaneous nondimensional evaporation timescale and $\mathcal{H}(r_v, r_l, r_s)$ is a Heaviside function indicating if evaporation or condensation occur, given by

$$\mathcal{H}(r_v, r_l, r_s) = \begin{cases} 1 & r_v \geqslant r_s \text{ or } r_l > 0 \\ 0 & \text{otherwise} \end{cases}, \tag{17}$$

and the (normalized) saturation vapor mixing ratio r_s is given by the Clausius-Clapeyron law

$$r_s = \exp(L_2\theta). \tag{18}$$

Note that the Reynolds number appears in the equations for temperature and water vapor as well. This is because we have chosen both the Prandtl and Schmidt numbers to be 1, which is realistic for these scalars. The Schmidt number for the liquid is taken to be infinite. Similar equations have been proposed to study the formation of precipitating convection [25] where vapor condenses to form liquid water droplets that can rain. Other simplified models include the model of Ref. [26], which assumes a piecewise-linear equation of state, and the "rainy Bénard" model of Ref. [27], where the full nonlinear equation of state is used, but the settling velocity of droplets is neglected. We also note that the initial conditions given by Eqs. (6)–(8) are only steady-state solutions of the governing equations (11)–(15) if both the diffusivity of vapor and the settling velocity of liquid water are switched off.

Following RMG20, we allow the settling velocity and the evaporation timescale to change as the liquid field evolves by maintaining the number density of droplets n to be constant during a simulation, such that $\tau_s = \tau_{s,0}[r_l/r_l^0]^{-1/3}$ and $v_p = v_{p,0}[r_l/r_l^0]^{2/3}$, where $\tau_{s,0}$ and $v_{p,0}$ are the values for $a = a_0$ and $r_l = r_l^0$. Choosing a base temperature T_b and a temperature scale ΔT, and assuming the two phases involved are water and air (see below), fixes the thermodynamic quantities

$$L_1 \equiv \frac{L_v r_s^0}{C_p \Delta T} \quad \text{and} \quad L_2 \equiv \frac{L_v \Delta T}{R_v T_b^2}. \tag{19}$$

Here C_p is the specific heat capacity of air, L_v is the enthalpy of vaporization of water, and R_v is the gas constant for water vapor. The other nondimensional parameters controlling the dynamics are the Froude number Fr, the Reynolds number Re, and the nondimensional shear rate S, given respectively by

$$\text{Fr}^{-2} \equiv \frac{g\Delta T/T_b h}{v_{p,0}^2}, \quad \text{Re} \equiv \frac{v_{p,0}h}{\nu}, \quad \text{and} \quad S \equiv \frac{\tilde{S}h}{v_{p,0}}, \tag{20}$$

where ν is the kinematic viscosity of air. The Reynolds number in this study is held fixed at Re $= 1000$. The nondimensional shear-rate S defined here is the inverse of the nondimensional settling velocity S_v defined, e.g., in Ref. [28]. Typical values of the settling velocity for droplets in mature cumulonimbus anvils are $O(1-5)$ m/s, and observations of asperitas clouds [11] suggest $\tilde{S} = O(0.01 - 0.02)$ s^{-1}. Taking $h = O(10)$ m, we have $S = O(0.1)$, consistent with the values used here. Since the nondimensional settling velocity is larger than unity, the effects due to the settling and evaporation occur on a faster timescale than that associated with the shear. This suggests that the instability due to shear is a secondary instability that modifies the mammatus instability of RMG20 and that parallels may be drawn to the influence of shear on Rayleigh-Taylor or Holmboe instabilities [29].
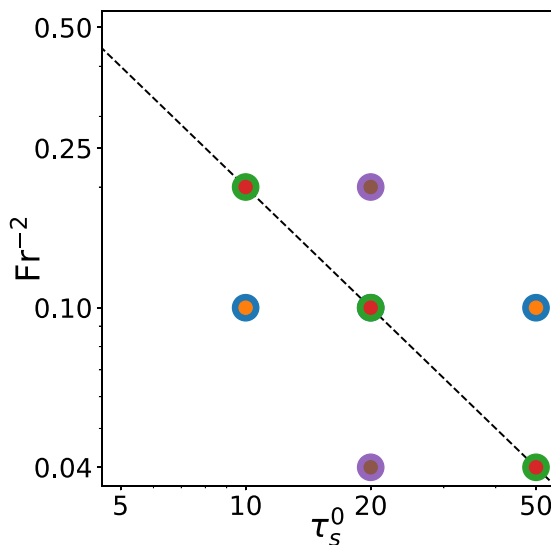
FIG. 3. A section of the parameter space explored in this work. The dashed line is the curve $\mathrm{Fr}^{-2} = 2\tau_{s,0}^{-1}$, corresponding to the behavior of water droplets in clouds, and the green-red markers are the specific combinations used. The blue-red markers are more general combinations. For each combination of $(\mathrm{Fr}^{-2}, \tau_{s,0})$ shown by the symbols, we perform simulations for several combinations of the shear rate S and the initial perturbation wavelength λ_x.

Using Eqs. (9) and (10) at the initial time, we have

$$\mathrm{Fr}^{-2}\tau_{s,0} = \frac{g\Delta T/T_b h}{v_{p,0}^2} \frac{C\rho_w a_0^2}{3r_l^0} \frac{v_{p,0}}{h} = \frac{3\nu\rho_d C\Delta T/T_b}{2\rho_w r_l^0}. \tag{21}$$

Except for the temperature scale ΔT, the base temperature T_b, and the initial liquid water content r_l^0 in the cloud, the quantities on the right-hand side of Eq. (21) are properties of the air-water system. Our simulations are performed for $r_l^0 = 0.3$, $\Delta T = 1$ K, and $T_b = 273$ K and thus the product $\mathrm{Fr}^{-2}\tau_{s,0}$ must have a fixed value, about 2 in our case, to be consistent with air-water properties in a cloud (see Fig. 3).

Our aim is to study how the instability that occurs due to this settling and evaporation of the liquid water droplets, giving lobelike structures for large $v_{p,0}$ and $r_{l,0}$ [5], is modified by the presence of shear. In particular, we ask whether shear can qualitatively change the very type of cloud type mammatus to asperitas. The requirement of significant shear could then explain the relative rarity of observations of asperitas clouds and therefore their very recent designation as a separate cloud type (as opposed to mammatus clouds which have been documented for over a century). We report results from two- and three-dimensional numerical simulations below.

The simulations are performed using the finite volume solver *Megha-5*, with second-order central differences in space and a second-order Adams-Bashforth timestepping scheme. For the liquid water Eq. (15), where the diffusion term is absent, we implement the Kurganov-Tadmor scheme [30] which enables nondiffusive advection, allowing for sharp gradients without incurring Gibbs oscillations. The numerical method was also described previously in RMG20. We fix Re = 1000. In 2D, the domain is of size 80×80 with a grid of 1024×1024 points, while in 3D the domain is of size $40 \times 40 \times 80$ with $256 \times 256 \times 512$ grid points. The timestep is $dt \leqslant 0.001$, such that the Courant-Friedrichs-Lewy number CFL $\leqslant 0.3$ even for the largest shear rates. We have checked that the results do not change qualitatively on doubling the number of grid points.
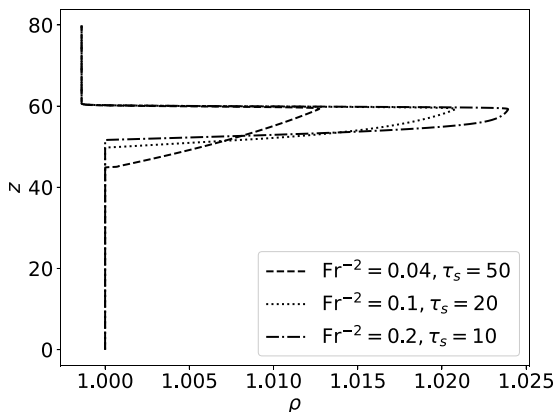
FIG. 4. The 1D density profiles for the three cloudlike cases considered (see Fig. 3). As in RMG20, smaller droplet sizes lead to narrower overhangs with a larger maximum density.

III. RESULTS AND DISCUSSION

A. Linear stability analysis

The governing equations (11)–(15) have a discontinuity at saturation. In order to perform linear stability analysis, therefore, we follow the same procedure as in RMG20. We run one-dimensional nonlinear simulations in the vertical coordinate and time for the settling and evaporation of liquid water into a dry subcloud layer and use the resulting density profile for our stability analysis. These profiles are slowly varying in time and, for the purposes of the stability analysis, can be assumed to be quasisteady. More details are available in RMG20. These density profiles, shown in Fig. 4, consist of "overhangs" of heavier fluid sandwiched between layers of lighter fluid at the cloudy-dry interface, with larger magnitudes and smaller widths for larger Fr^{-2} and smaller τ_s (i.e., smaller droplet sizes).

We examine the stability of the resulting "base state" by linearizing the nondimensional governing equations for the vorticity

$$q = \frac{\partial u}{\partial z} - \frac{\partial w}{\partial x}$$

and the density ρ, which are

$$\frac{\partial q}{\partial t} + U \frac{\partial q}{\partial x} = \frac{1}{Re} \nabla^2 q + \frac{1}{Fr^2} \frac{\partial \rho}{\partial x}, \tag{22}$$

$$\frac{\partial \rho}{\partial t} + U \frac{\partial \rho}{\partial x} = \frac{1}{Re} \nabla^2 q - w(D\bar{\rho}), \tag{23}$$

where $D \equiv d/dz$ and $U \equiv U(z) = S(z_0 - z)$ is the background shear velocity, while $\bar{\rho}(z)$ is the background density obtained from one-dimensional nonlinear simulations of the governing equations.

Expanding q and ρ in normal modes

$$(q, \rho) = (\hat{q}, \hat{\rho}) \exp[i(kx - \omega t)], \tag{24}$$

and noting that incompressibility requires
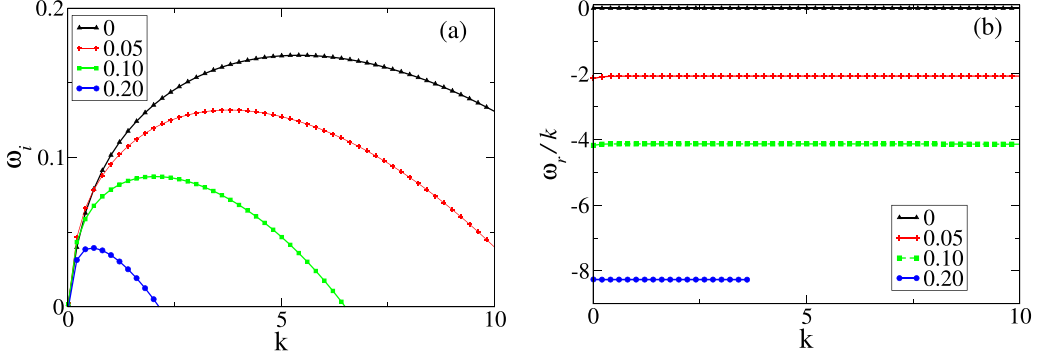
$$ik\hat{u} + D\hat{w} = 0, \tag{25}$$

FIG. 5. (a) The growth rate ω_i and (b) the phase velocity ω_r/k as a function of the horizontal perturbation wave number k and the shear rate S for density profiles obtained with parameters $\mathrm{Fr}^{-2} = 0.2$, $\tau_s = 10$. Results for other combinations of parameters show the same qualitative behavior.

gives

$$\hat{q} = \frac{i}{k}\left(D^2 - k^2\mathcal{I}\right)\hat{w}. \tag{26}$$

Equations (22) and (23) in normal form, written for $\hat{w}$ and $\hat{\rho}$, become

$$\frac{\partial}{\partial t}\left(D^2 - k^2\mathcal{I}\right)\hat{w} + ikU\left(D^2 - k^2\mathcal{I}\right)\hat{w} = \frac{1}{\mathrm{Re}}\left(D^2 - k^2\mathcal{I}\right)^2\hat{w} + \frac{ik}{\mathrm{Fr}^2}\hat{\rho}, \tag{27}$$

$$\frac{\partial}{\partial t}\hat{\rho} + ikU\hat{\rho} = \frac{1}{\mathrm{Re}}\left(D^2 - k^2\mathcal{I}\right)^2\hat{\rho} - \hat{w}(D\bar{\rho}). \tag{28}$$

We see that the only imaginary terms are due to the background shear $U(z)$, as expected. Equations (27) and (28) are solved for the complex growth rate ω using the Chebyshev decomposition employed in RMG20. The growth rate and the dispersion relation are plotted in Fig. 5. Figure 5(a) shows that the maximum growth rate occurs for smaller wave numbers with increasing shear; thus, shear damps out small-scale instabilities. Figure 5(b) shows that the phase speed scales with the shear rate S. We note that the flow velocity and the phase velocity coincide [i.e., $U(z) = \omega_r/k$], at $z \approx z|_{\rho_{\max}}$. It is this interaction at the critical layer that leads to the instability.

We note that while the linear stability results are qualitatively consistent with the results from nonlinear simulations to be presented below, the caveats described in RMG20 apply here, too, so we do not make quantitative comparisons. In particular the base flow itself evolves over time, and we have used a density profile at an arbitrary time to perform the linear stability analysis.

B. Results from 2D simulations

RMG20 find that, in the absence of shear, mammatus lobe formation can be predicted from 2D simulations, and nothing changes qualitatively between these and 3D simulations. We therefore begin our investigations with 2D simulations. The application of shear sets a preferred horizontal direction and, as discussion in Sec. I, is known to cause the formation of salt sheets parallel to the direction of the shear flow [18–21,31] in thermohaline and settling-driven convection. In the 2D simulations, this leads to a planar interface.

Equations (11)–(15) are specialized to two dimensions by setting $v \equiv 0$, and $\partial/\partial y \equiv 0$. We find, in general agreement with previous work on related systems, that the introduction of shear smooths out small-scale perturbations [19,20]. We also find that increasing droplet sizes, corresponding here to lower Fr^{-2} and larger $\tau_{s,0}$, supports larger lobe sizes. As derived in Eq. (21), we have an inverse relationship between the nondimensional parameters Fr^{-2} and $\tau_{s,0}$, which for the air-water system,
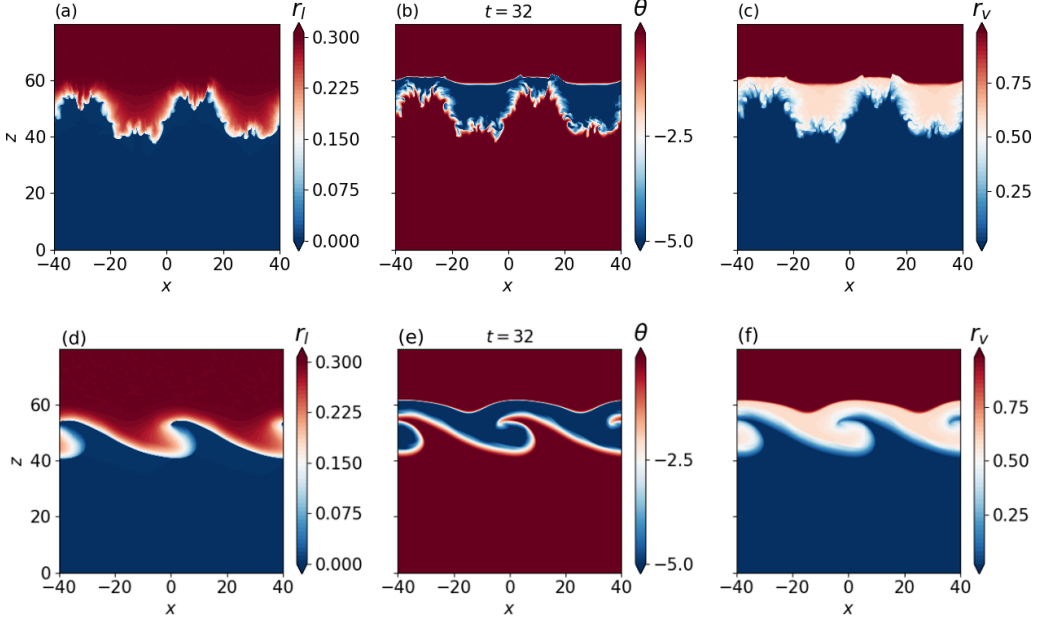
FIG. 6. Shear dampens the growth of small wavelength instabilities. The flow parameters are Re $= 1000$, $r_l^0 = 0.3$, Fr$^{-2} = 0.1$, $\tau_s = 20$, $z_0 = 60$, with [(a)–(c)] $S = 0$ and [(d)–(f)] $S = 0.2$ liquid mixing ratio [(a) and (d)], the temperature [(b) and (e)] and the vapour mixing ratio [(c) and (f)] are plotted at the time indicated.

and our chosen variables, appears as the dashed line in Fig. 3). Indeed, in general the parameters Fr^{-2} and $\tau_{s,0}$ may not obey this relationship. Examples of such systems include spray drying in the pharmaceutical industry (see, e.g., Ref. [32]) and heterogeneous catalysis using microspheres [33,34] that may be found in chemical engineering industry. We therefore consider cases with and without the inverse relationship between Fr^{-2} and $\tau_{s,0}$, to mimic "cloudlike" and "non-cloud-like" flows, respectively, and our simulation parameters are shown by the markers in Fig. 3. We note that our derivation of the inverse relationship is restricted to small droplets. For larger droplet sizes, the settling velocity is overestimated by the Stokes drag law, while the phase-change timescale is underestimated if nonlinear ventilation effects are neglected [24].

The simulations in 2D have an initial perturbation of the cloudy-dry interface given in Eqs. (3). Similar initial conditions were used in RMG20, where it was found that the presence of noise does not affect the results greatly. It was also found that in the absence of shear, the imposed sinusoidal perturbation grows faster than the "natural" mode that may be excited if the ratio of the imposed wavelength to the "natural" wavelength is not too large (see Sec. 3 in RMG20); whereas for sufficiently large λ_x, short wavelength modes are excited in addition to the growth of the imposed wavelength. Our main results are described below.

1. Suppression of small wavelength instabilities by shear

For very low shear rates S, the system displays a mammatus-like instability. For very high shear rates ($S \geqslant 0.4$, not shown), all instabilities are suppressed and the cloudy-dry interface becomes flat as it descends. Intermediate shear rates, we find, suppress the short wavelength modes preferentially. These findings are consistent with results for settling and evaporation driven instabilities without shear and the influence of shear on sedimentation-driven instabilities without evaporation. First, in instabilities driven by settling and evaporation (without shear) [5], the fastest growing modes, at least in the early stages, occur for smaller droplet sizes and thus (in our notation
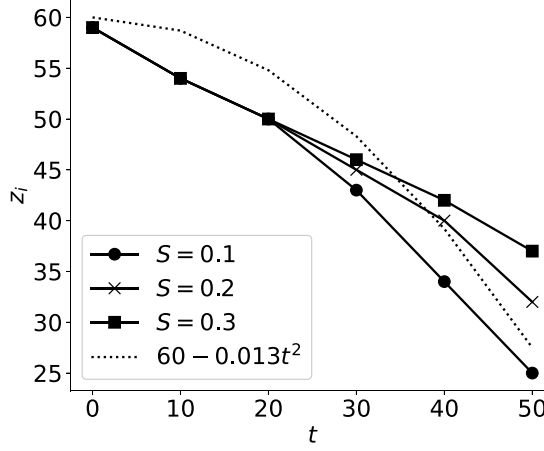
FIG. 7. The location of the cloudy-dry interface, z_i, as a function of time as the shear rate S is varied, with $Fr^{-2} = 0.1$, $\tau_{s,0} = 20$, $\lambda_x = 20$. Shear suppresses the settling and evaporation-driven instability, leading to smaller mixing rates.

here) larger Fr^{-2} and smaller τ_s. We note that this is in contrast to unsheared settling-driven instabilities without evaporation, where the growth rates are larger for larger settling velocities [12,13]. Second, in double-diffusive and sedimentation-driven instabilities without evaporation, Konopliv *et al.* [19] find, considering linearized transient optimal growth, that shear more strongly suppresses faster growing modes. In instabilities driven by settling and evaporation, these are the small-scale instabilities, and small-scale perturbations may therefore be expected to be preferentially suppressed.

Figure 6 compares the shape of the clouds with and without shear at a typical time of $t = 32$. The left panels show the liquid water content, which would correspond to the visual appearance of the cloud. In all the results shown, the initial base of the cloud has been located at $z_0 = 60$. Water droplets have descended well below this by the time shown, and an instability has grown and evidently become nonlinear. The stabilizing effect of shear on small scales is apparent. For $S = 0$, small-scale instabilities appear in addition to the imposed wavelength $\lambda_x = 40$. For identical
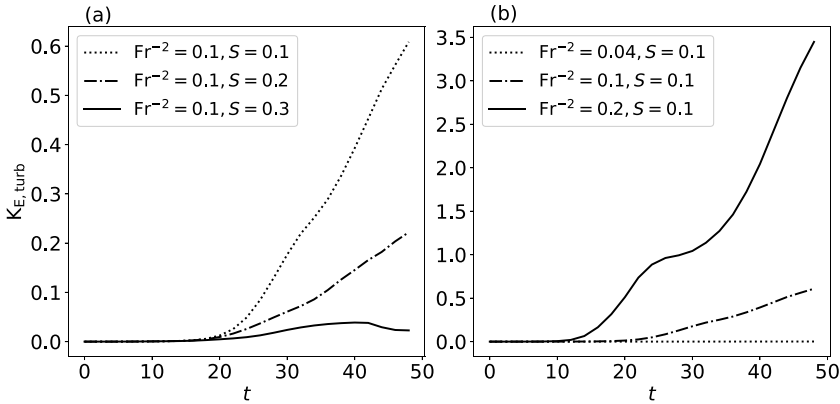

FIG. 8. The turbulent kinetic energy (see text for definition) in the "cloudlike" cases as a function of time for (a) different S with $Fr^{-2} = 0.1$ and (b) different Fr^{-2} with $S = 0.1$, with $\lambda_x = 20$. Note that the curve for $Fr^{-2} = 0.1$, $S = 0.1$ appears in both subfigures.
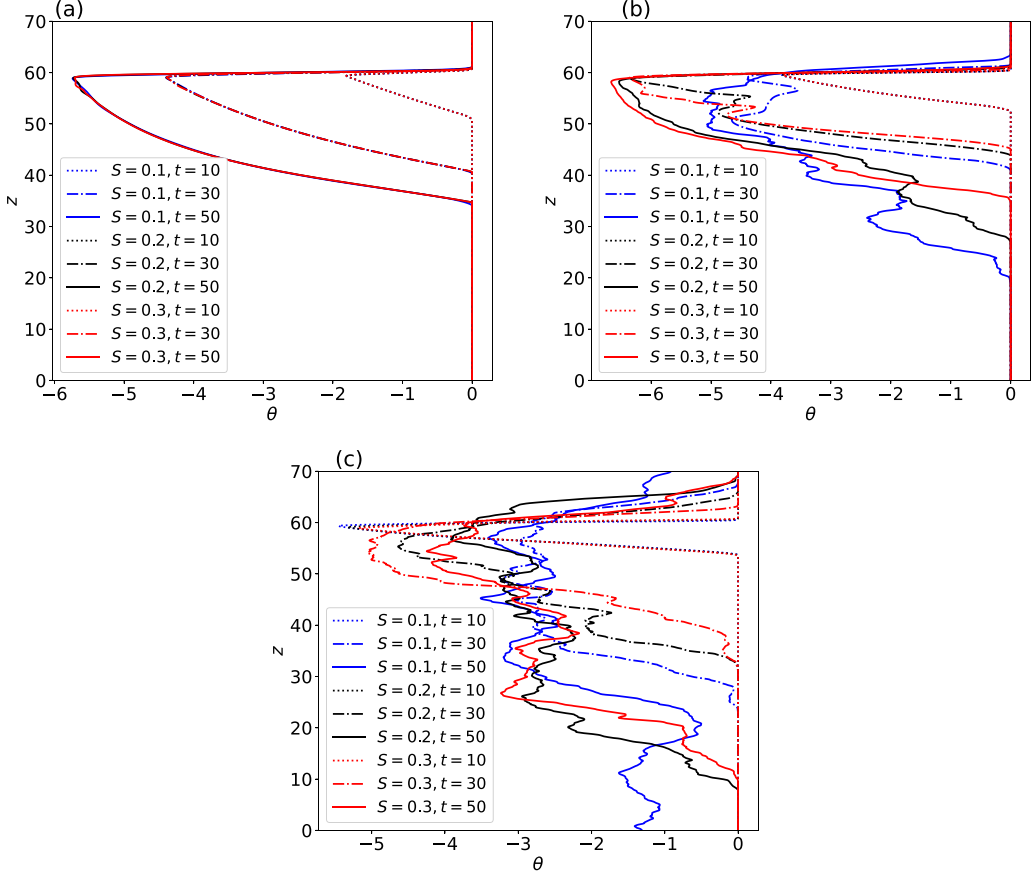
FIG. 9. Horizontally averaged profiles of the temperature θ, plotted at three times and three values of the shear rate S (a) $Fr^{-2} = 0.04$, (b) $Fr^{-2} = 0.1$, and (c) $Fr^{-2} = 0.2$ with $\lambda_x = 20$. In each case, shear suppresses the instability, leading to smaller mixed layer depths.

initial conditions but with $S = 0.2$, the small-scale instabilities are suppressed and only the $\lambda_x = 40$ mode is seen. Moreover, as is to be expected, the structures are now tilted by the shear. The middle panels show the temperature profiles. Evaporative cooling is evident (blue regions in the figure) in the portion of the cloud where droplets have descended from the original cloud base. In this region, the water vapor content (right panels) is higher than that of dry air, as expected from evaporation. There is a broad correspondence in the shape of structures displayed by the three physical quantities, although they are different in detail. We will see that in three dimensions, there are greater differences between the structures displayed by the three scalars.

The rate at which the cloudy-dry interface moves in the $-z$ direction is a measure of the rate of mixing by the flow. Since the region $z < z_0$ is initially dry ($r_v = 0$) we locate this interface at $z = z_i$ at which the horizontally averaged vapor mixing ratio $\bar{r}_v(z)$ takes on a threshold value of 0.1. In Fig. 7, we plot the location of this interface for three values of shear. At early times, the instability develops similarly in the three cases, and mixing levels are similar. But at later times, larger shear suppresses the development of the instability structures and retards the mixing.

The suppression of flow instabilities by shear is also evidenced in Fig. 8, where we plot the domain-averaged turbulent kinetic energy

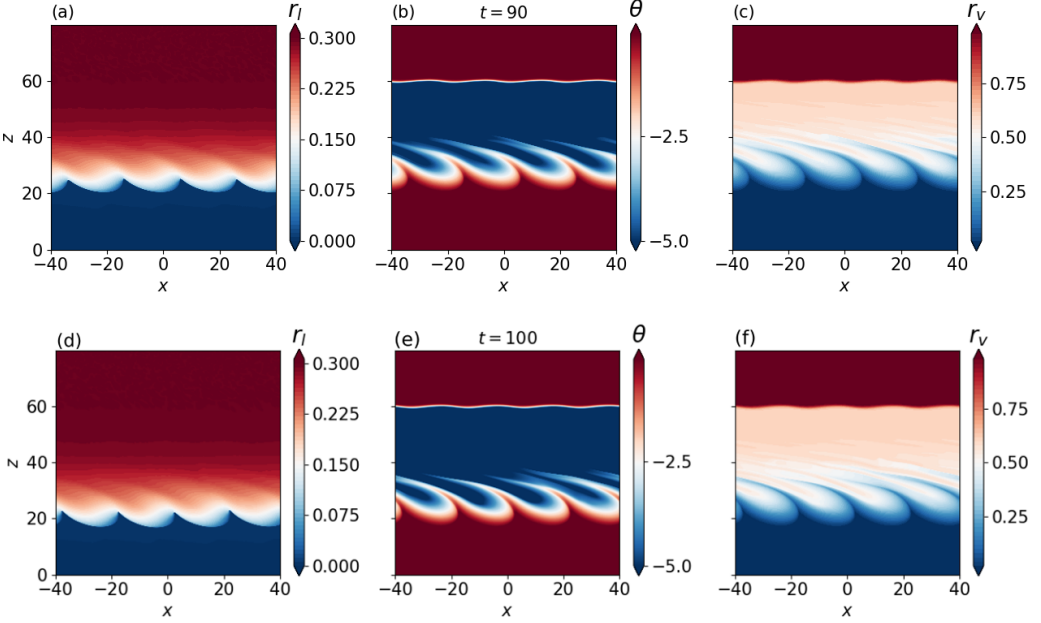$$K_{E,\text{turb}} = K_E - K_E(t = 0),$$

FIG. 10. For sufficiently large shear, the tendency of the instability to grow and the tendency of the shear to suppress growth balance each other, leading to lobes that maintain their size and approximately their shape as they descend. The parameters are $Fr^{-2} = 0.04$, $\tau_s = 50$, $S = 0.1$, $z_0 = 60$, $\lambda_x = 20$, and the liquid mixing ratio [(a) and (d)], the temperature [(b) and (e)] and the vapour mixing ratio [(c) and (f)] are plotted at the times indicated.

where the base value due to the background shear (the kinetic energy at $t = 0$) is subtracted. For each combination of "cloudlike" Fr^{-2} and τ_s, we see that larger shear leads to smaller kinetic energy.

We examine the evolution of the mixed layers by plotting the horizontally averaged temperature excess in Fig. 9, showing that the rate at which the mixed layers grow is inversely related to the shear rate S. We also note that the mixed layers grow only for $z < z_0$ for large droplet sizes (small $Fr^{-2} = 0.04, 0.1$) while for $Fr^{-2} = 0.2$, the turbulent flow penetrates the stably stratification at $z = z_0$ and thus the mixed layer grows in both directions from $z = z_0$. Profiles of other variables show similar behavior.

At significant shear rate and for large droplet sizes (i.e., smaller Fr^{-2} and larger τ_s than seen in Fig. 6), the instabilities grow rather slowly, so the sheared lobes maintain their appearance as they descend for tens of flow units, as seen in Fig. 10. The lobe sizes that can be maintained in this way are larger for higher shear rates. We remark that the structures seen are not Lagrangian objects that are descending. They are constantly being renewed by evaporation and regeneration of the instability while the shape is being maintained. For small droplet sizes, on the other hand, the flow becomes turbulent and structure shapes are not maintained over significant durations. This may be surmised from Figs. 7 and 12, both of which show the influence of different parameters on the mixing rate.

2. Effect of deviation from "cloudlike" parameters

As discussed in Sec. II, "cloudlike" cases have $Fr^{-2}\tau_{s,0} \approx 2$ (see Fig. 3), while this relation may not hold in other systems of interest with a settling and reacting scalar component. To ask how a departure from cloudlike physical parameters will affect the instability, we explore in Fig. 11, the consequence of keeping $Fr^{-2} = 0.1$ while changing $\tau_{s,0}$, i.e., moving along the horizontal in Fig. 3. The "cloudlike" case ($Fr^{-2} = 0.1$, $\tau_{s,0} = 20$) is expected to be similar to the lower panel
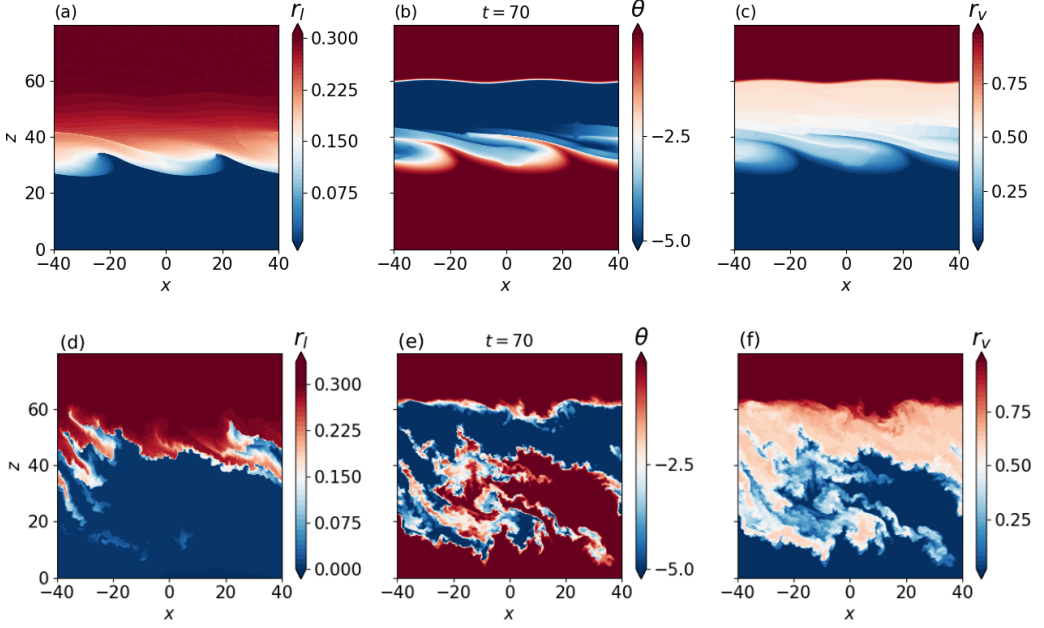
FIG. 11. With all other parameters held fixed, slower evaporation than "cloudlike," i.e., $\tau_s = 50$, (a) leads to a lobelike instability, while faster evaporation than "cloudlike," i.e., $\tau_s = 10$, (b) leads to small-scale instabilities which lead to much greater mixing and larger fluxes of vapor and energy (although not liquid; see text). The parameters are $\mathrm{Fr}^{-2} = 0.1$, $S = 0.25$, $z_0 = 60$, $\lambda_x = 40$, and the liquid mixing ratio [(a) and (d)], the temperature [(b) and (e)] and the vapour mixing ratio [(c) and (f)] are plotted at the times indicated.

of Fig. 6. Smaller droplets (lower $\tau_{s,0}$) evaporate faster, leading to larger scalar fluxes of vapor and energy, and lower liquid water content, given that it is the evaporation of the liquid that is the source of kinetic energy in the flow. Interestingly, therefore, the liquid in this case occupies a
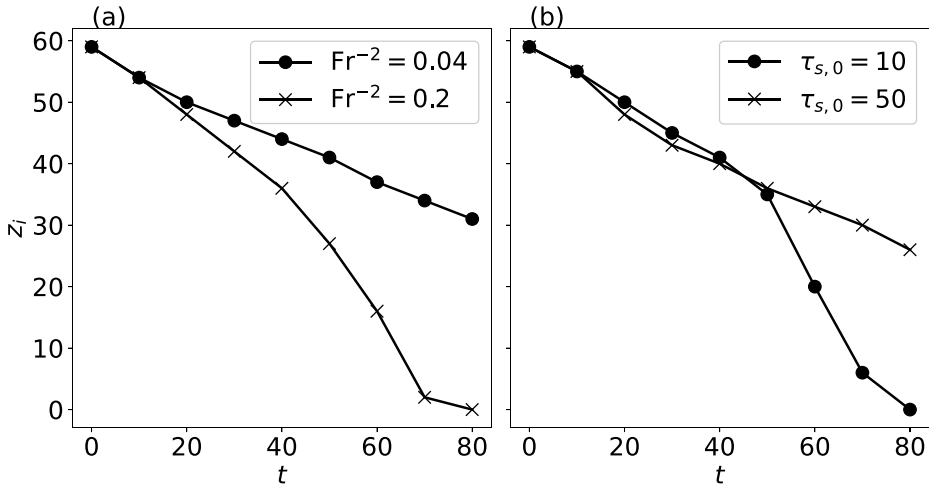

FIG. 12. The location of the cloudy-dry interface z_i, defined as in Fig. 7, as a function of time for (a) $\tau_{s,0} = 20$ and two values of Fr^{-2}, and (b) $\mathrm{Fr}^{-2} = 0.1$, and two values of $\tau_{s,0}$, showing that the mixing is faster for smaller τ_s and larger Fr^{-2}. The other parameters are $S = 0.25$ and $\lambda_x = 20$.
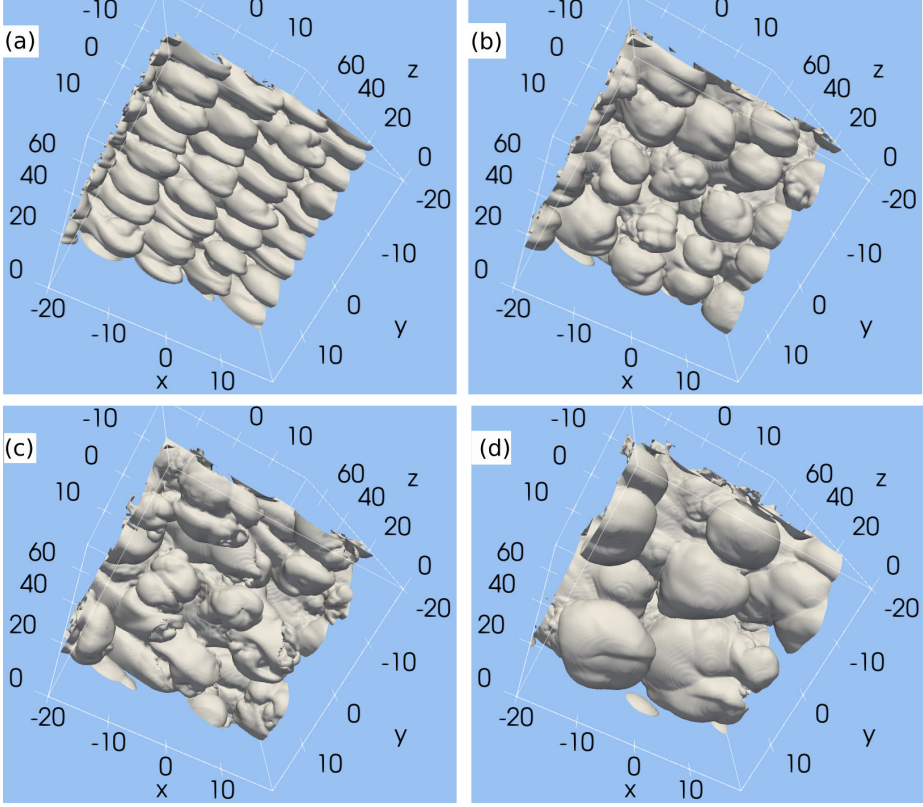
FIG. 13. The growth of the sheared lobes with $S = 0.05$, $\lambda_x = 20$ and (a) $\lambda_y = 5$, (b) $\lambda_y = 10$, (c) $\lambda_y = 20$, and (d) $\lambda_y = 40$. The other parameters are $Fr^{-2} = 0.04$ and $\tau_s = 50$. The isosurfaces are plotted at $r_l = 0.01$ and time $t = 80$. The lobes in (d) have reached $z \approx 10$ and developed while those in (a) have only reached $z = 20$. Refer to Fig. 14 with all the same parameters except a larger shear rate.

smaller region below the "cloud" as compared to the temperature and vapor fields, which means that the visual appearance of such a flow would not be indicative of the other scalars. The structures in temperature and vapor are less well formed and more chaotic in appearance than in a cloudlike case. In general, for the same Fr^{-2}, larger values of $\tau_{s,0}$ lead to (lobelike) instabilities of larger wavelengths, while smaller values of τ_s lead to smaller-scale instabilities; conversely, for the same $\tau_{s,0}$, larger values of Fr^{-2} (i.e., stronger buoyancy) result in instabilities of smaller wavelengths, while weak buoyancy (smaller Fr^{-2}) leads to larger length-scale instabilities. We see thus that flows made up of larger droplets are more likely to take on an asperitas-like appearance and also be longer lived. Further evidence for this is given in Fig. 12. Here we plot the horizontally averaged vertical location z_i of the "cloudy"-dry interface as Fr^{-2} and $\tau_{s,0}$ are varied. A slope of -1 on these graphs would indicate a mixing layer growing at the same rate as the initial particle settling velocity. The behavior we see may be explained by noting that both smaller τ_s and larger Fr^{-2} are representative of smaller droplets, which evaporate faster for a given r_l, leading to higher subcloud cooling, and therefore a greater role for buoyancy. At higher levels of buoyancy, observations in settling-driven two-component systems without phase change show (e.g., Ref. [13]) that the velocity of the interface is higher, and this is consistent with what we see. The additional physics in our case is that we do not impose the buoyancy forcing externally, but it gets generated as a result of the thermodynamics of phase change.
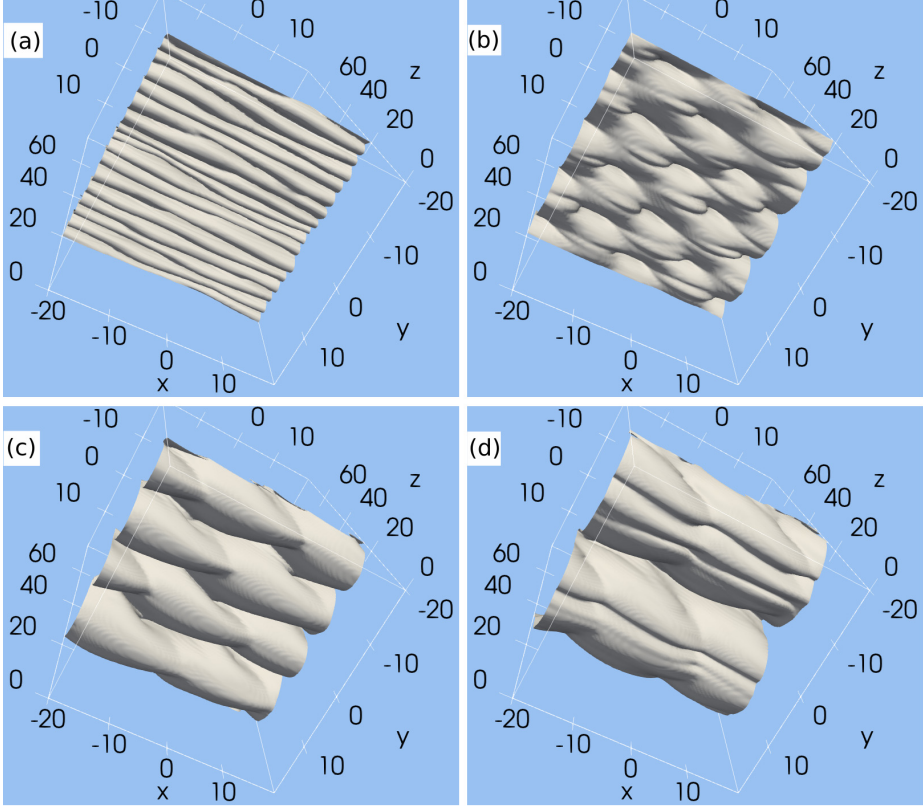
FIG. 14. The growth of the sheared lobes at the same time $t = 80$ and with the same parameters as Fig. 13 except with a larger shear rate $S = 0.1$. The isosurfaces are plotted at $r_l = 0.01$ as in Fig. 13 and show that the instability is more pronounced for when the x and y wavelengths of the perturbations are large and comparable to each other.

C. Three-dimensional simulations

A systematic analysis of the growth rate of the instability in 3D as the horizontal wavelengths are varied will be presented elsewhere, since the main aim at present is to bring the physics to light. For this purpose it is sufficient to present results from cases with $\mathrm{Fr}^{-2} = 0.04$, $\tau_s = 50$ ("cloudlike"), while varying the shear rate S and the initial perturbation wavelengths λ_x and λ_y. Due to computational constraints, the simulations were performed with half the grid resolution (i.e., twice the grid spacing) as the 2D simulations and with horizontal domains of 40×40.

As discussed in Sec. I, shear leads to the formation of "salt sheets" in double-diffusive or sediment-driven convection. For small shear rates, the mammatus-lobe instability results. For large shear rates [see Eq. (1)], the interface evolves to become homogeneous in the x direction, leading to "liquid sheets." For intermediate shear, as in 2D, the nature of the lobes that form is determined by the competition between the growth rate and the homogenising effect of shear.

The central effect of shear is as follows. RMG20 found that the growth rates of linear instabilities driven by settling and evaporation is larger for smaller droplet sizes (of smaller settling velocities), which lead to smaller instability wavelengths. However, as we have seen, the homogenizing effects of shear suppress instabilities of the small wavelengths. As a result, when shear is nonzero, larger wavelengths have larger growth rates. This is seen in Fig. 13 which shows isosurfaces at $r_l = 0.01$ at a typical time. A small value of liquid water content is chosen to plot the isosurfaces, so that the
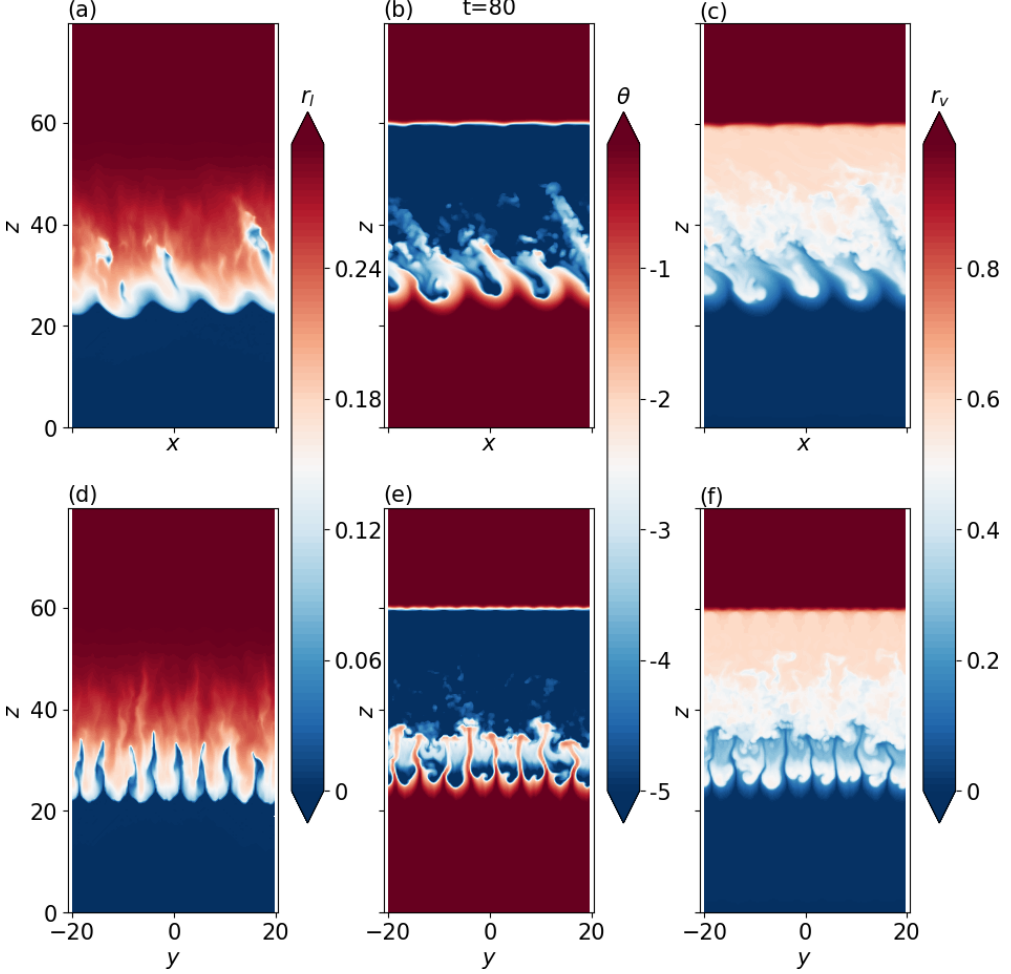
FIG. 15. Two views of the liquid mixing ratio r_l [(a) and (c)], the temperature θ [(b) and (d)], and the vapor mixing ratio r_v [(c) and (f)] on [(a)–(c)] x-z planes at $y = 0$ and [(d)–(f)] y-z planes at $x = 0$. The parameters are $S = 0.05$, $\mathrm{Fr}^{-2} = 0.04$, $\tau_s = 50$, $\lambda_x = 20$, $\lambda_y = 5$, as in Fig. 13(a). Refer to Fig. 17 with all the same parameters except a larger shear rate.

images may correspond closely to the visual appearance of the cloud. It is seen that (a) larger shear rates lead to smaller growth rates, other things being held constant, and (b) larger wavelengths lead to more developed lobes at a given time for the same shear. We also note that the effect of the shear is most obviously seen in the wave number of the instability in the y direction, which is twice as large as the imposed y wave number.

Figures 13 and 14 and the corresponding cross sections of the flow variables, plotted in Figs. 15–18, show that the equivalent of "salt sheets" are formed for the larger shear rate $S = 0.1$. Thus, the shear rate required to homogenise the flow along the direction of the shear flow is smaller in 3D than in 2D. A revealing aspect of the 3D simulations is that high shear organizes the structures into elongated formations rather than the bloblike appearance which was seen in mammatus clouds. Moreover, when the perturbation wavelengths in the two horizontal directions are very different [Figs. 13(a) and 14(a)], higher shear leads to thinner and feebler structures. In the light of Figs. 13 and 14, we may return to Fig. 1. It is apparent that suitably designed initial conditions could lead
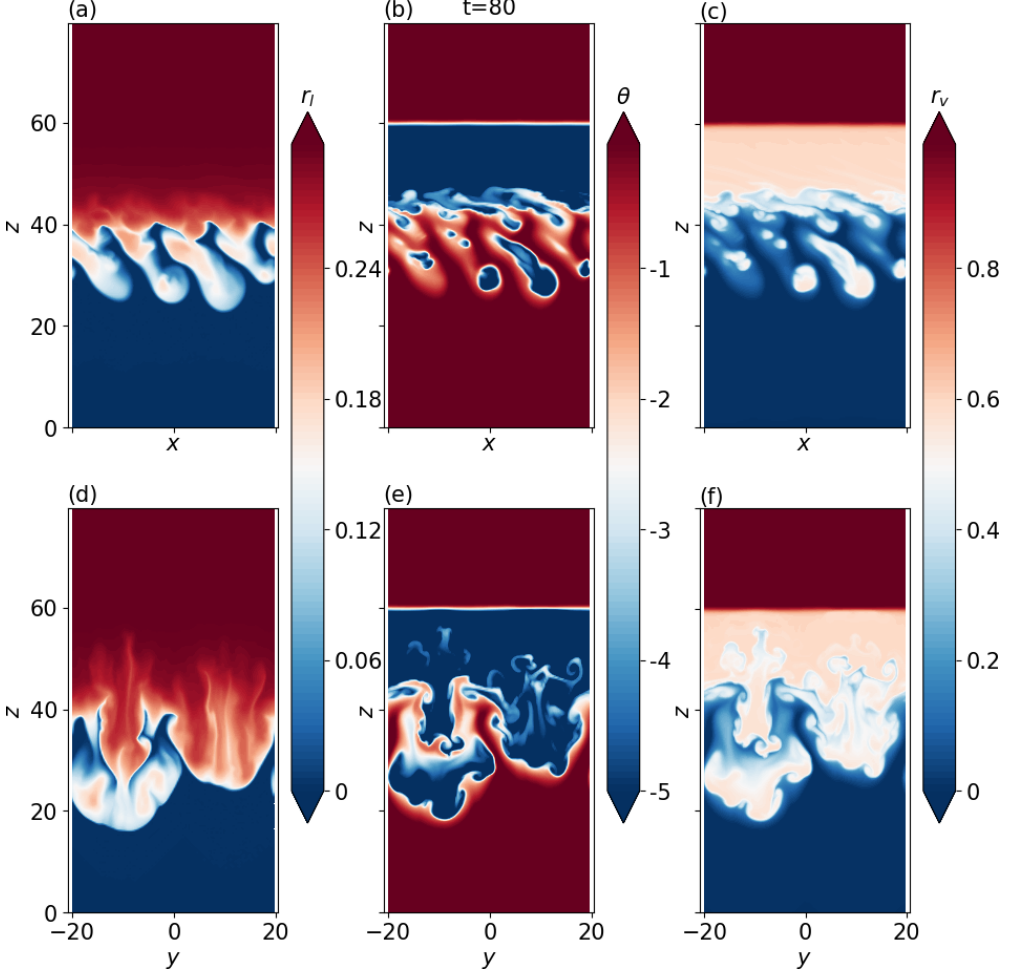
FIG. 16. Two cross sections of the simulations shown in Fig. 13(d) of the liquid mixing ratio r_l [(a) and (c)], the temperature θ [(b) and (d)], and the vapor mixing ratio r_v [(c) and (f)] on [(a)–(c)] x-z planes at $y = 0$ and [(d)–(f)] y-z planes at $x = 0$. The parameters are $S = 0.05$, $\mathrm{Fr}^{-2} = 0.04$, $\tau_s = 50$, $\lambda_x = 20$, $\lambda_y = 40$. Refer to Fig. 18 with all the same parameters except a larger shear rate.

to numerical formations of the kind seen in real asperitas clouds. The effect of shear, and of the wavelength of the dominant perturbation, on the 3D instability structures is made more evident in the cross-sectional views shown in Figs. 15–18. First we notice that there is far less structure in the plane of the shear (the x-z plane) than in the y-z plane. Structures are broadly aligned in the streamwise direction, and this is reminiscent of streamwise streaks in standard Couette flow which are generated by the nonmodal growth of perturbations. Second, the structures look remarkably periodic despite the flow being quite turbulent, which is evident from the plots of the vapor field r_v. Since descent dominates the liquid field, we do not see much turbulence here.

IV. CONCLUSIONS AND OUTLOOK

We have studied the effects of shear on the instability driven by the evaporation of a scalar component that settles under gravity. In both two and three dimensions, shear suppresses the development of the settling and evaporation driven instability, analogously with similar findings for fingering
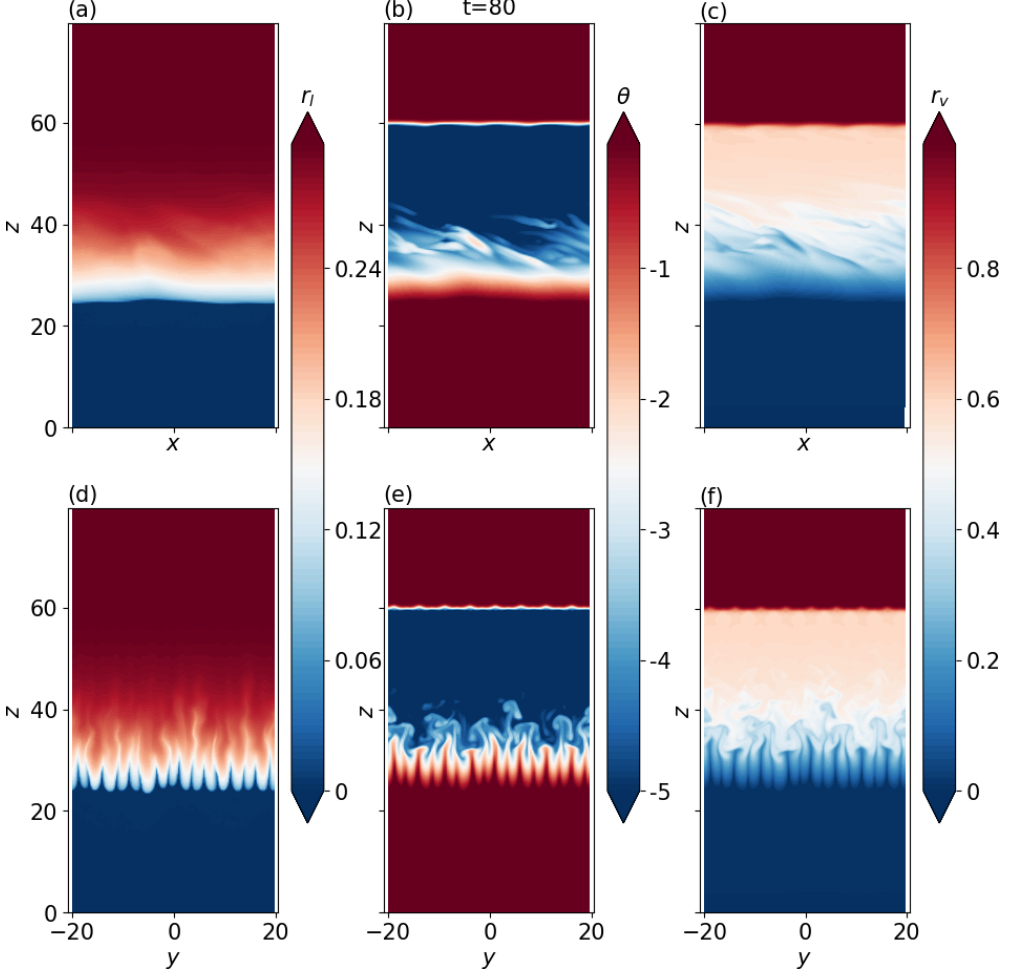
FIG. 17. Cross sections of the liquid mixing ratio r_l [(a) and (c)], the temperature θ [(b) and (d)], and the vapor mixing ratio r_v [(c) and (f)] on [(a)–(c)] x-z planes at $y = 0$ and [(d)–(f)] y-z planes at $x = 0$, for the same parameters as in Fig. 15 except with a larger shear rate $S = 0.1$. At late times, the flow is homogeneous in the x direction.

and sedimentation driven instabilities. We showed, additionally, that small-scale instabilities are suppressed preferentially by the shear. We argued that this is because shear more strongly suppress the fastest growing sedimentation-driven modes which, when evaporation is also present, are of small scale. We then showed the existence in 2D of a balance between shear and the instability which preserves the size and shape of descending lobes. Last, we showed that when Fr^{-2} and $\tau_{s,0}$ are varied independently, smaller Fr^{-2} and larger $\tau_{s,0}$ lead to lobelike instabilities and smaller scalar fluxes.

In 3D, we found that the instabilities, at least when the initial perturbation wavelength is externally imposed, rapidly lead to the sheetlike structures previously observed in the sedimentation-driven and double-diffusive fingering regimes. For small shear rates, we showed that distorted lobelike structures resembling asperitas clouds can be generated. For large shear rates, the instabilities become homogeneous in the direction of the shear flow, producing a closer resemblance to clouds in Fig. 1(b). Since shear almost always exists in the troposphere (as also evidenced in the few known measurements associated with asperitas observations), this suggests shear-influenced settling and evaporation as a possible mechanism for the formation of asperitas clouds.
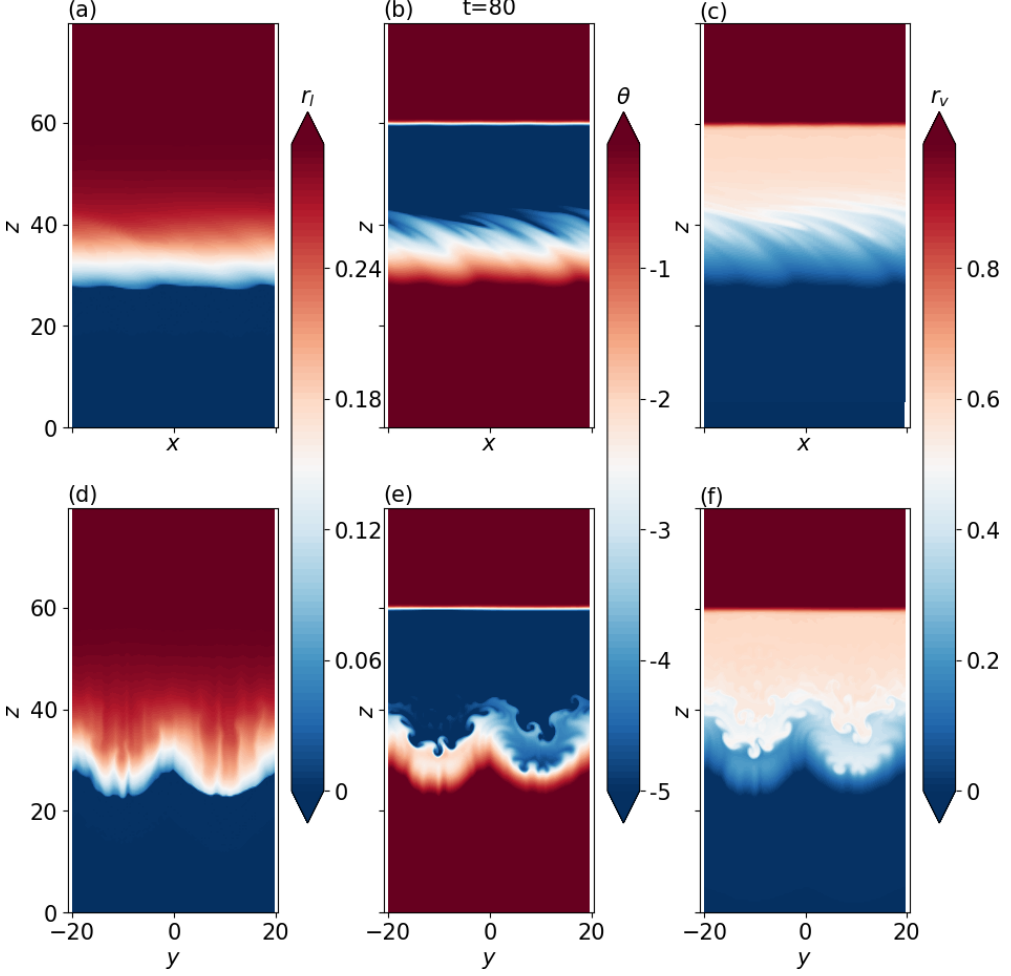
FIG. 18. Cross sections of the liquid mixing ratio r_l [(a) and (c)], the temperature θ [(b) and (d)], and the vapor mixing ratio r_v [(c) and (f)] on [(a)–(c)] x-z planes at $y = 0$ and [(d)–(f)] y-z planes at $x = 0$, for the same parameters as in Fig. 16 except with a larger shear rate $S = 0.1$. At late times, the flow is homogeneous in the x direction.

The mechanism laid down here makes specific predictions about why asperitas clouds are rarer [11] than mammatus clouds. The formation of mammatus clouds by settling and evaporation requires sufficiently large droplet sizes as well as sufficiently large liquid water content. These criteria also apply to the formation of asperitas clouds. We have shown that shear is an important additional ingredient in the formation of asperitas-like clouds. And that when the shear rates are either too small (and the clouds resemble mammatus clouds) or too large (when the different lobes merge in the direction of shear and the structures are unable to grow to significant depth), asperitas clouds may not form. In the case of mammatus clouds, RMG20 found that the results were qualitatively the same in 2D and 3D, and bloblike protruberances are seen in both. In asperitas clouds, however, 3D simulations are necessary to distinguish between bloblike and undulating formations. It is shown that the latter are more likely at higher shear.

We note that our simulations are highly idealized and the caveats laid down in RMG20 apply here. In particular, our Reynolds number of Re = 1000 is significantly smaller than realistic values.

We have applied a given wave number in each direction in our simulations, whereas a real asperitas cloud would obviously display a combination of these. In fact it would be an interesting exercise to emulate asperitas shapes seen in the atmosphere by prescribing initial perturbations which contain a spectrum of wavelengths. Furthermore, as with mammatus clouds, the settling and evaporation-driven mechanism may not explain all occurrences of asperitas clouds.

Some avenues for future work are evident. We mention two here.

(i) The optimal combination of Fr^{-2} and τ_s, if they can be varied independently, that maximises the flux of a given scalar quantity (with and without externally imposed shear and in 2D and 3D) would be relevant for optimising certain processes in the chemical engineering industry. Such results for settling-driven and double-diffusive convection have been obtained, e.g., in Ref. [13]. Given our focus on the elucidating the mechanism and on the visual patterns formed by the instability, a systematic parametric study is beyond the scope of this work. However, the results in Figs. 7 and 12 may be considered initial findings in that direction. We believe our formulation of settling and evaporation-driven, shear modulated, convection in terms of the three nondimensional parameters Fr^{-2}, τ_s and S has laid the foundation for this effort.

(ii) Double-diffusive and sedimentation driven instabilities are known to lead to "staircases," i.e., to alternating horizontal layers containing, and devoid of, the scalar component(s) (see, e.g., Refs. [31,35,36]). It would be of great interest to find whether such staircases are possible in a system where one scalar component can evaporate.

[1] D. M. Shultz, K. M. Kanak, J. M. Straka, R. J. Trapp, B. A. Gordon, D. S. Zrnić, G. H. Bryan, A. J. Durant, T. J. Garrett, P. M. Klein, and D. K. Lilly, The mysteries of mammatus clouds: Observations and formation mechanisms, J. Atmos. Sci. **63**, 2409 (2006).

[2] K. M. Kanak and J. M. Straka, An idealized numerical simulation of mammatus-like clouds, Atmos. Sci. Lett. **7**, 2 (2006).

[3] K. M. Kanak, J. M. Straka, and D. M. Schultz, Numerical simulation of mammatus, J. Atmos. Sci. **65**, 1606 (2008).

[4] T. J. Garrett, C. T. Schmidt, S. Kihlgren, and C. Cornet, Mammatus clouds as a response to cloud-base radiative heating, J. Atmos. Sci. **67**, 3891 (2010).

[5] S. Ravichandran, E. Meiburg, and R. Govindarajan, Mammatus cloud formation by settling and evaporation, J. Fluid Mech. **899**, A27 (2020).

[6] International Cloud Atlas (2017), WMO No. 407, Section 2.2.2.4.7, World Meteorological Organisation, https://cloudatlas.wmo.int/en/clouds-supplementary-features-asperitas.html.

[7] Photograph by Ave Maria Mõistlik, downloaded from Wikimedia Commons under a Creative Commons Attribution-ShareAlike 3.0 license, https://commons.wikimedia.org/w/index.php?curid=6581290.

[8] Photograph by Agathman, downloaded from Wikimedia Commons under a Creative Commons Attribution 3.0 license, https://commons.wikimedia.org/wiki/File:Stratocumulus_stratiformis_opacus_lacunosus_undulatus_asperitas.jpg.

[9] The Cloud Appreciation Society, PO Box 81, Somerton, Somerset TA11 9AY, United Kingdom, https://cloudappreciationsociety.org.

[10] Video by Alex Schueth (July 2014), https://www.youtube.com/watch?v=Jz7BgxrVmiQ.

[11] R. G. Harrison, G. Pretor-Pinney, G. J. Marlton, G. D. Anderson, D. J. Kirshbaum, and R. J. Hogan, Asperitas—A newly identified cloud supplementary feature, Weather **72**, 132 (2017).

[12] P. Burns and E. Meiburg, Sediment-laden fresh water above salt water: Linear stability analysis, J. Fluid Mech. **691**, 279 (2012).

[13] P. Burns and E. Meiburg, Sediment-laden fresh water above salt water: Nonlinear simulations, J. Fluid Mech. **762**, 156 (2014).

[14] X. Yu, T.-J. Hsu, and S. Balachandar, Convective instability in sedimentation: Linear stability analysis, J. Geophys. Res.: Oceans **118**, 256 (2013).

[15] X. Yu, T.-J. Hsu, and S. Balachandar, Convective instability in sedimentation: 3-d numerical study, J. Geophys. Res.: Oceans **119**, 8141 (2014).

[16] G. Carazzo and M. A. Jellinek, A new view of the dynamics, stability and longevity of volcanic clouds, Earth Planet. Sci. Lett. **325–326**, 39 (2012).

[17] G. Carazzo and A. M. Jellinek, Particle sedimentation and diffusive convection in volcanic ash-clouds, J. Geophys. Res.: Solid Earth **118**, 1420 (2013).

[18] T. Radko, J. Ball, J. Colosi, and J. Flanagan, Double-diffusive convection in a stochastic shear, J. Phys. Oceanogr. **45**, 3155 (2015).

[19] N. Konopliv, L. Lesshafft, and E. Meiburg, The influence of shear on double-diffusive and settling-driven instabilities, J. Fluid Mech. **849**, 902 (2018).

[20] P. Garaud, A. Kumar, and J. Sridhar, The interaction between shear and fingering (thermohaline) convection, Astrophys. J. **879**, 60 (2019).

[21] P. H. Sichani, C. Marchioli, F. Zonta, and A. Soldati, Shear effects on scalar transport in double diffusive convection, J. Fluids Eng. **142**, 121105 (2020).

[22] An Update on the Asperatus Cloud, Cloud Appreciation Society (2011), https://cloudappreciationsociety. org/asperatus-update/.

[23] M. R. Maxey and J. J. Riley, Equation of motion for a small rigid sphere in a nonuniform flow, Phys. Fluids **26**, 883 (1983).

[24] H. Pruppacher and J. Klett, *Microstructure of Atmospheric Clouds and Precipitation* (Springer Netherlands, Amsterdam, 2010), pp. 10–73.

[25] G. Hernandez-Duenas, A. J. Majda, L. M. Smith, and S. N. Stechmann, Minimal models for precipitating turbulent convection, J. Fluid Mech. **717**, 576 (2013).

[26] O. Pauluis and J. Schumacher, Idealized moist rayleigh-benard convection with piecewise linear equation of state, Commun. Math. Sci. **8**, 295 (2010).

[27] G. K. Vallis, D. J. Parker, and S. M. Tobias, A simple system for moist convection: The rainy-bénard model, J. Fluid Mech. **862**, 162 (2019).

[28] B. J. Devenish, P. Bartello, J.-L. Brenguier, L. R. Collins, W. W. Grabowski, R. H. A. IJzermans, S. P. Malinowski, M. W. Reeks, J. C. Vassilicos, L.-P. Wang, and Z. Warhaft, Droplet growth in warm turbulent clouds, Q. J. R. Meteorol. Soc. **138**, 1401 (2012).

[29] J. R. Carpenter, E. W. Tedford, E. Heifetz, and G. A. Lawrence, Instability in stratified shear flow: Review of a physical interpretation based on interacting waves, Appl. Mech. Rev. **64**, 60801 (2011).

[30] A. Kurganov and E. Tadmor, New high-resolution central schemes for nonlinear conservation laws and convection-diffusion equations, J. Comput. Phys. **160**, 241 (2000).

[31] A. Traxler, S. Stellmach, P. Garaud, T. Radko, and N. Brummell, Dynamics of fingering convection. part 1 small-scale fluxes and large-scale instabilities, J. Fluid Mech. **677**, 530 (2011).

[32] N. Fu, M. W. Woo, and X. D. Chen, Single droplet drying technique to study drying kinetics measurement and particle functionality: A review, Dry. Technol. **30**, 1771 (2012).

[33] J. Ji, P. Zeng, S. Ji, W. Yang, H. Liu, and Y. Li, Catalytic activity of core-shell structured cu/fe3o 4@sio2 microsphere catalysts, Catal. Today **158**, 305 (2010).

[34] W. Hu, B. Liu, Q. Wang, Y. Liu, Y. Liu, P. Jing, S. Yu, L. Liu, and J. Zhang, A magnetic double-shell microsphere as a highly efficient reusable catalyst for catalytic applications, Chem. Commun. **49**, 7596 (2013).

[35] T. Radko, *Double-Diffusive Convection* (Cambridge University Press, Cambridge, UK, 2012).

[36] R. Ouillon, P. Edel, P. Garaud, and E. Meiburg, Settling-driven large-scale instabilities in double-diffusive convection, J. Fluid Mech. **901**, A12 (2020).